F. nucleatum facilitates oral squamous cell carcinoma progression via GLUT1-driven lactate production

Jiwei Sun,[a,b,c,f] Qingming Tang,[a,b,c,f] Shaoling Yu,[a,b,c] Mengru Xie,[a,b,c] Wenhao Zheng,[a,b,c] Guangjin Chen,[a,b,c] Ying Yin,[a,b,c] Xiaofei Huang,[a,b,c] Keqi Wo,[a,b,c] Haoqi Lei,[a,b,c] Junyuan Zhang,[a,b,c] Qian Wan,[d,e] and Lili Chen[a,b,c,*]

[a]Department of Stomatology, Union Hospital, Tongji Medical College, Huazhong University of Science and Technology, Wuhan, 430022, China
[b]School of Stomatology, Tongji Medical College, Huazhong University of Science and Technology, Wuhan, 430030, China
[c]Hubei Province Key Laboratory of Oral and Maxillofacial Development and Regeneration, Wuhan, 430022, China
[d]Hubei Key Laboratory of Natural Medicinal Chemistry and Resource Evaluation, School of Pharmacy, Huazhong University of Science and Technology, 13 Hangkong Road, Wuhan, 430030, Hubei, China
[e]Institute of Brain Research, Huazhong University of Science and Technology, 13 Hangkong Road, Wuhan, 430030, Hubei, China

eBioMedicine
2023;88: 104444
Published Online xxx
https://doi.org/10.1016/j.ebiom.2023.104444

Summary

Background Tumor-resident microbiota has been documented for various cancer types. Oral squamous cell carcinoma (OSCC) is also enriched with microbiota, while the significance of microbiota in shaping the OSCC microenvironment remains elusive.

Methods We used bioinformatics and clinical sample analysis to explore relationship between *F. nucleatum* and OSCC progression. Xenograft tumor model, metabolic screening and RNA sequencing were performed to elucidate mechanisms of pro-tumor role of *F. nucleatum*.

Findings We show that a major protumorigenic bacterium, *F. nucleatum*, accumulates in invasive margins of OSCC tissues and drives tumor-associated macrophages (TAMs) formation. The mechanistic dissection shows that OSCC-resident *F. nucleatum* triggers the GalNAc-Autophagy-TBC1D5 signaling, leading to GLUT1 aggregation in the plasma membrane and the deposition of extracellular lactate. Simultaneous functional inhibition of GalNAc and GLUT1 efficiently reduces TAMs formation and restrains OSCC progression.

Interpretation These findings suggest that tumor-resident microbiota affects the immunomodulatory and protumorigenic microenvironment via modulating glycolysis and extracellular lactate deposition. The targeted intervention of this process could provide a distinct clinical strategy for patients with advanced OSCC.

Funding This work was supported by the National Natural Science Foundation of China for Key Program Projects (82030070, to LC) and Distinguished Young Scholars (31725011, to LC), as well as Innovation Team Project of Hubei Province (2020CFA014, to LC).

Keywords: Oral squamous cell carcinoma; *F. nucleatum*; Tumor-associated macrophage; GLUT1; Autophagy

Introduction

Oral squamous cell carcinoma (OSCC) is a prevalent subtype of head and neck squamous cell carcinoma (HNSCC).[1–3] Despite progress in the diagnosis and treatment of OSCC, the 5-year survival rate remains low due to metastasis or recurrence.[4,5] Cohort studies have suggested that, in addition to the genetic, epigenetic, and stromal microenvironment elements, the features of the microbiota within tissues are associated with the hallmarks of cancer, including risks, pathological types, and prognosis.[6–10] Likewise, given that OSCC originates in the microbiota-enriched oral cavity, the microbiota emerges as a non-negligible potential mediator regulating OSCC progression.[11–14] *F. nucleatum* is a gram-negative anaerobic bacterium and has been suggested as a major protumorigenic bacterium compared with other oral bacteria.[15,16] However, as the constituent species of OSCC microbiota, how *F. nucleatum* affects the progression of OSCC remains largely unexplored.

*Corresponding author. Department of Stomatology, Union Hospital, Tongji Medical College, Huazhong University of Science and Technology, 1277 Jiefang Avenue, Wuhan, 430022, China.
E-mail address: chenlili1030@hust.edu.cn (L. Chen).
[f]Jiwei Sun and Qingming Tang contributed equally to this article.

Research in context

Evidence before this study

Multiple types of microbiota derived from oral cavity have been detected in malignant lesions including colorectal cancer, oropharyngeal cancer and breast cancer. However, there are fewer studies focused on role of oral microbiota in OSCC development. The direct mechanisms for the pro-tumor effect of microbiota have been clarified, including chemo-resistance, proliferation and epithelium–mesenchymal transition. But how microbiota participate in the reshaping of tumor immune microenvironment still remains unexplored.

Added value of this study

Bioinformatic and clinical analysis were performed to elucidate that large amounts of *F. nucleatum* were observed to colonize in OSCC invasive margins, along with accumulation of tumor-associated macrophages (TAMs). Xenograft tumor model further confirmed local invasion of OSCC could be triggered largely by formation of TAMs in invasive margins. RNA sequencing and metabolic analysis were conducted to clarify *F. nucleatum*–mediated upregulation of GLUT1 was mainly responsible for formation of acidic local microenvironment, which was proper for induction of TAMs. Mechanistic research observed *F. nucleatum*–activated GalNAc-Autophagy-TBC1D5 signaling pathway could explain GLUT1 membrane translocation and subsequent lactate deposition in tumor microenvironment.

Implications of all the available evidence

Amounts of *F. nucleatum* in clinical detection on OSCC samples might be a powerful index to indicate potential OSCC invasion. Double targeting at GalNAc and GLUT1 might be applied as a novel treatment for advanced OSCC patients by remodeling of tumor immune microenvironment.

The previous study has shown that *F. nucleatum* lectin Fap2 recognizes the host N-acetylgalactosamine (GalNAc), a glycoprotein expressed on cell surface mediating the binding between bacteria and tumor cells by carbohydrate moiety, and helps this bacterium abundantly localize in tumor tissues.[17] Notably, *F. nucleatum* can drive metabolism and epithelial–mesenchymal transition (EMT) of multiple types of tumors, including colorectal, breast, and oropharyngeal tumors, supporting cancerous cell growth.[9,18,19] Nevertheless, these identified mechanisms are limited to physiopathological processes within cells and fail to account for the impacts on the microenvironment associated with tumor progression. *F. nucleatum* colonization has been suggested to ignite acute innate immune responses, especially macrophage infiltration in the microenvironment.[20] Given that M2-like tumor-associated macrophages (TAMs) are vital in promoting tumor invasion,[21,22] these reports suggested that *F. nucleatum*-driven microenvironmental macrophage activation could be implicated in promoting tumor invasion.

In this study, we sought to elucidate the effect of *F. nucleatum* on the OSCC microenvironment and its relevance to OSCC progression. We identified *F. nucleatum* as a highly-enriched species in OSCC samples. *F. nucleatum* tends to colonize in the invasive margins of OSCC. Mechanistic dissection showed that *F. nucleatum* promotes aggregation of Glucose Transport 1 (GLUT1), a crucial rate-limiting factor for cellular glucose uptake and metabolism, in the plasma membrane and glycolysis via activating the GalNAc-Autophagy-TBC1D5 signaling axis, resulting in extracellular lactate deposition and M2-like TAMs formation. Concurrent inhibition of GalNAc and GLUT1 leads to M1-like anti-tumor macrophage formation in the microenvironment and regression of OSCC progression. These findings provide new prospects for the targeted therapeutic strategy for patients with advanced OSCC.

Methods

Clinical samples

The clinical samples used in this study were all originated from one single center. Calculations for the sample size of this cross-sectional study were performed using the function Confidence Intervals for One Proportion in software PASS v15.08. Results showed that at least 75 patients should be enrolled in this study. Thus, a total of 80 paired OSCC clinical tumor and adjacent normal tissues were randomly acquired from pathologically diagnosed OSCC patients at the maxillofacial Department, the Second Xiangya Hospital of Central South University (Changsha, China), from Oct 2019 to Sep 2020. The recruited patients included male and female OSCC patients covering the age interval of 31–73 without subjective rejection. Informed consents have been signed by patients involved in our research. Tissue specimens were all stored in liquid nitrogen within 15 min after being resected from patients to ensure stabilization of RNA and protein. Pathological and clinical information, including sex, age, clinical and pathological diagnosis and classification, TNM staging, lymph node metastasis status, oral hygiene and health status, and life habits, have been recorded in detail.

In vivo oral cancer colonization and *F. nucleatum* intervention

A total of 520 male C3H mice (4–6 weeks old) were purchased from the Beijing HFK Bioscience, maintained in an SPF environment and fed with antibiotic-free food and water *ad libitum*. Ethical guidelines from the Institutional

Animal Care and Use Committee of Tongji Medical College (IACUC) were followed during animal-related experiments. Animals used in this study were randomly allocated into different groups using the method simple random sampling. Mice were then subcutaneously injected with 5×10^5 SCC-7 tumor cells. After the tumor volume reached at 500 mm^3, mice were randomly divided into two groups for further treatment. The sample size was estimated and determined based on sample size calculation with previous study, the assay sensitivity, expected heterogeneity of samples, as well as published literatures,[23] and five mice each group was statistically enough in our cases. Mice in the experimental group were then subcutaneously injected with 5×10^7 *F. nucleatum*. In contrast, mice in the control group were injected with equivalent PBS. 14 days after the intervention, mice were sacrificed for subsequent experiments.

Effect of macrophages on *F. nucleatum* related oral cancer progression

Subcutaneous tumor models were established as described above. Mice were then randomly divided into 4 groups: 1) PBS, 2) 5×10^7 *F. nucleatum* only, 3) 5×10^7 *F. nucleatum* and Clodronate liposomes (Clodronateliposomes, CP-005-005), 4) 5×10^7 *F. nucleatum* and PBS liposomes. 20 μL liposomes were injected subcutaneously into xenograft tumors two times before injection of *F. nucleatum* into the same region.

Therapeutic strategies on inhibition of *F. nucleatum*-related oral cancer progression

Subcutaneous tumor models were established as described above. When xenograft tumors reached up to 500 mm^3, Mice were then randomly divided into 5 groups: 1) PBS, 2) 5×10^7 *F. nucleatum* only, 3) 5×10^7 *F. nucleatum* and BAY-876 (MCE), 4) 5×10^7 *F. nucleatum* and PNA solution (Sigma), 5) 5×10^7 *F. nucleatum* and a combination of BAY-876 and PNA. BAY-876 at a concentration of 3 mg/kg was injected into the local tumor every 3 days, and PNA solution (80 μg/mL) was locally injected following the above instructions. A combination of the two solutions was injected for combined therapeutic application. After the above treatments for 14 days, mice were sacrificed to compare tumor weight and volume (n = 5 animals per treatment per group). The tumor weight and length were detected by digital calipers to calculate tumor volumes.

Bacteria culture and fluorescent labeling

Fusobacterium nucleatum (*F. nucleatum*) strain ATCC-25586 was grown on Columbia agar plates supplemented with defibrinated sheep blood (PB003A, Beijing Luqiao, China) for 3–6 days in an anaerobic chamber at 37 °C. For fast bacteria enrichment, *F. nucleatum* colonies were cultured anaerobically in Thayer Martin medium (BD) for 48–72 h. To detect *F. nucleatum* directly, SYTO-9 (Invitrogen, S34854) was applied for fluorescent labeling according to the manufacturer's instructions. Tumor cells co-cultured with SYTO-9 labeled *F. nucleatum* for 60 and 120 min were then fixed with 4% PFA for 10–20 min, permeabilized with 0.1% Triton X-100, and subsequently nuclear-stained with DAPI.

Cell culture

Human primary oral keratinocytes (OKCs) derived from fresh oral mucosa tissues during operative resection, human OSCC cell lines CAL27 (ATCC Cat# CRL-2095, RRID: CVCL_1107), SCC15 (ATCC Cat# CRL-1623, RRID: CVCL_1681) and SCC25 (ATCC Cat# CRL-1628, RRID: CVCL_1682), and human monocyte cell line THP-1 (ATCC Cat# TIB-202, RRID: CVCL_0006) were cultured in air-humidified cell incubator with 5% CO2 at 37 °C. Keratinocyte medium (Promocell), DMEM high glucose medium (Hyclone) and RPMI-1640 medium (Hyclone) supplemented with 10% fetal bovine serum (Gibco) were utilized for amplification of OKCs, tumor cell lines and THP-1 cells, respectively. Before stimulating cells with *F. nucleatum* or experimental drugs, the regular medium was replaced with a serum-free medium for subsequent cell culture to avoid experimental bias. For stimulation of *F. nucleatum* to tumor cells, untreated live *F. nucleatum* was diluted into PBS, followed by co-culturing with tumor cells at proper MOI of 10, 50 and 100 for further experiments. For targeted inhibition of GLUT1, BAY-876 (MCE, HY-100017) was pretreated on tumor cells before interventions at 50 nM for 24 h. For a wide-range blockade of MCTs to obstruct lactate digestion, 7ACC2 (MCE, HY-D0713) was applied at 10 μmol/L for pretreatment of M0 macrophages. To inhibit the glycolytic process, 2-DG (MCE, HY-13966) was pretreated on tumor cells overnight at the concentration of 20 mmol/L. For inhibition of AKT, SC79 (MCE, HY-18749) was pretreated on tumor cells at 8 μmol/L. For mTOR inhibition, 3BDO (MCE, HY-U00434) was pretreated on tumor cells at the concentration of 20 μmol/L. For inhibition of TLR4, TAK-242 (MCE, HY-11109) was pretreated on tumor cells at 50 nmol/L. For inhibition of protein synthesis, CHX (sigma, 66-81-9) was pretreated on tumor cells at the concentration of 50 μg/mL. For inhibition of autophagy, 3-MA (MCE, HY-19312) was pretreated on tumor cells at 12 mmol/L. For activation of autophagy, rapamycin (MCE, HY-10219) was pretreated on tumor cells at 50 nmol/L. For blockade of cell surface GalNAc, PNA (Sigma, L0881) was applied on tumor cells at 80 μg/mL. For inhibition of lysosome activity for degradation of membrane GLUT1, Bafilomycin A1 (MCE, HY-100558) was added into the culturing medium at 500 nM for another 24 h. For inhibition of proteasome activity, MG-132 (MCE, HY-13259) was applied on tumor cells at the concentration of 150 nM. For activation of ubiquitin-proteasome system, RAMB4 (MCE, HY-W054146) was used at 25 μM for 24 h.

Indirect and direct cell co-culture

Two types of cell co-culture experiments were performed in this study. 1). OSCC tumor cells were seeded on culture plates and were stimulated by live *F. nucleatum* at proper MOI (1:50) for 24 h. Culturing supernatant was then extracted and filtered by a 0.22 μm strainer for the depletion of bacteria. A filtered medium was used to stimulate THP-1-derived macrophages for another 48 h. 2). Corning Transwell insert chamber (0.4 μm pore size) was used for the direct cell co-culture system. Polarized macrophages were seeded in the upper chamber, and tumor cells were seeded in the lower chamber for co-culturing for 48 h.

Reanalysis of bacterial sequencing data from public database

The raw 16S rRNA sequencing data of OSCC clinical samples from projects PRJNA352375 and SRP097643 were acquired from Sequence Reads Archive (SRA) and preprocessed by Novogene. Software QIIME (Quantitative Insights into Microbial Ecology) package version 1.9.1 was applied to explore downstream information, including subclassifying of samples, plotting of bacterial taxonomy, calculation of species richness, and alpha and beta diversity indices. Principal Component Analysis (PCoA) method was applied to analyze bacterial community variations between different groups. Differentially enriched bacterial taxa and genus were acquired by two different analyzing methods, Metastat and Simper.

TCGA-HNSCC dataset analysis

The Cancer Genome Atlas (TCGA) database is a curated and annotated public database containing sequencing data for tumor samples. RNA sequencing data for 544 head and neck squamous cell carcinoma (HNSCC) patients was acquired from TCGA, and the relative expression level of *GLUT1* between cancerous and non-cancerous tissues was analyzed and compared.

Mass untargeted spectrometric metabolomics analysis

For the profile of variations in tumor metabolism, culturing supernatant samples collected from *F. nucleatum*-stimulated CAL27 cells were filtered and vortexed for purification, sonicated at 4 °C for 20 min and maintained at –20 °C later for protein precipitation. Finally, purified samples were delivered to BGI Tech for subsequent sequencing. High-resolution mass spectrometer Q Exactive (Thermo Fisher Scientific, USA) was used to collect metabolomic data, and subsequent data processing and analysis were conducted by The Compound Discover 3.1 (Thermo Fisher Scientific, USA).

Transwell assay

Corning Transwell insert chamber (5.0 μm pore size) was used for transwell assay following the indicated protocols. Briefly, OSCC cells dispersed into a serum-free medium were seeded onto the matrigel (BD) on the surface of the upper chamber, and polarized macrophages treated under different conditions were seeded on the lower well for 24 h. For *F. nucleatum* mediated macrophage recruitment, macrophages with the serum-free medium were seeded onto the upper chamber, and *F. nucleatum* suspension was added into the lower chamber at the same time overnight. Later, cells on Transwell chamber membranes were fixed with 4% PFA for 15 min, followed by staining of crystal violet for another 15 min. Images were then randomly captured under a microscope.

Si RNA transfection

Specific si-RNA and non-specific control oligonucleotides were custom-made and acquired from GenePharma. Si-RNAs were designed to target human GLUT1 and ATG5 genes, and two efficient targets were prepared for each gene. Lipofectamine3000 (ThermoFisher, L3000) was implemented following the manufacturers' instructions for transfection treatment. Co-culture of tumor cells, Lipofectamine3000 and si-RNA with recommended concentrations for 24–48 h was carried out before medium refresh. The efficiency for gene knockdown manipulation could maintain 3–6 days examined by qPCR detection.

Plasmids transfection

To overexpress TBC1D5 in OSCC cell lines, the insert sequence was constructed and cloned in vector puc57 and used for transfection of OSCC cells with lentivirus. CAL27 cells were transfected with lentivirus at the MOI of 10. Puromycin (2 μg/mL) was applied to select stably transfected cells. The empty vector was used as a control.

RNA sequencing

Total RNA extraction was carried out on CAL27 cells stimulated by *F. nucleatum* or PBS, and three repeats were prepared for each group. Samples were then sent to BGI Tech for subsequent sequencing. Finally, raw reads which were more than 50 bp and conformed to quality control standards were selected for further analysis. FPKM values were applied for gene normalization and quantification. Gene Ontology (GO) and Kyoto Encyclopedia of Genes and Genomes (KEGG) were used to analyze biological functions based on differentiated expression genes between the two groups.

Isolation of proteins in cellular membrane and cytoplasm

Total cellular proteins were extracted and isolated into the membrane and cytosolic proteins using a membrane and cytosol protein extraction kit following indicated instructions (ThermoFisher, 89842). Briefly, collected cells were lysed with Reagent A containing PMSF

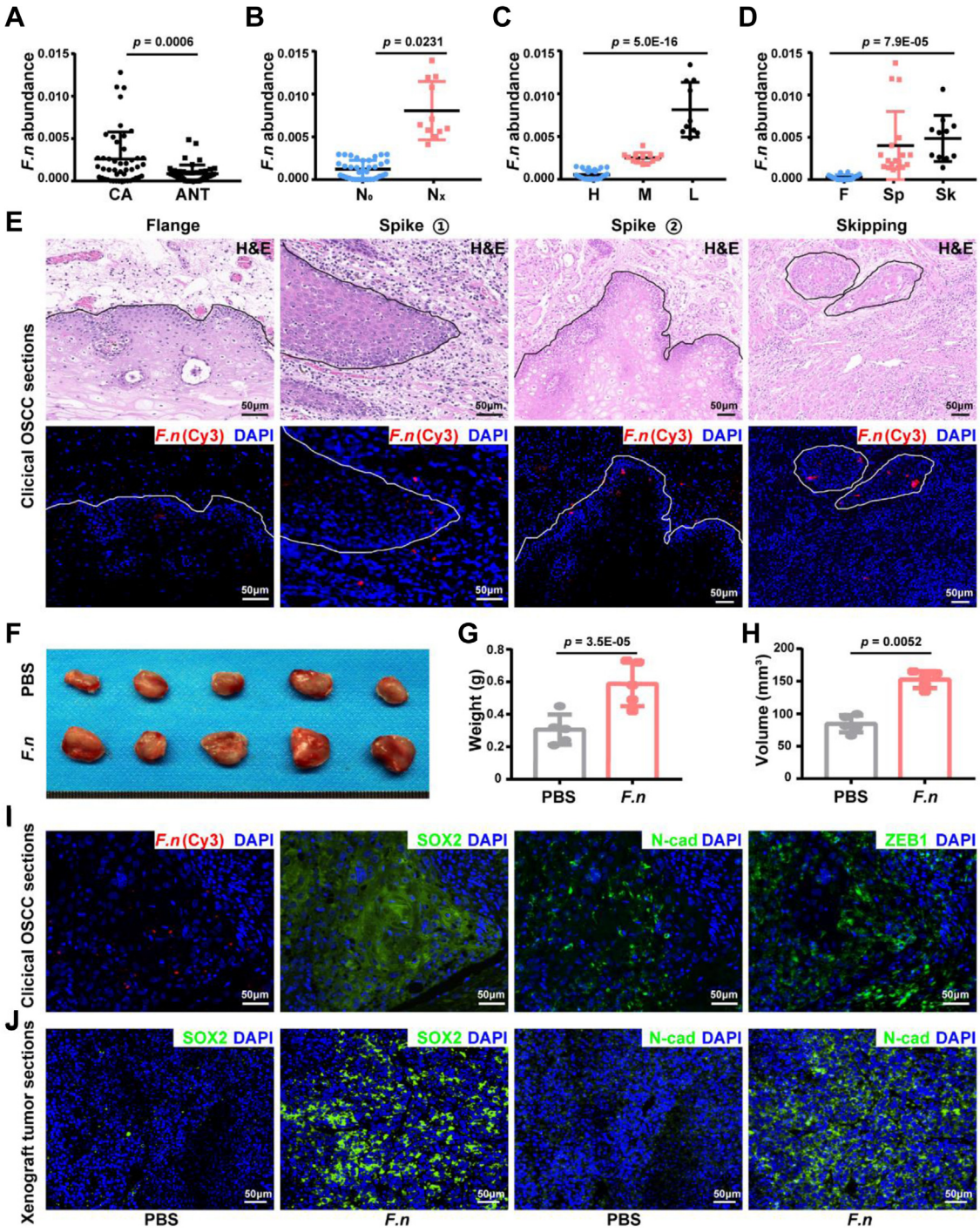

***Fig. 1: F. nucleatum* aggregates at the invasive margin of OSCC and correlates with tumor invasion.** (A) *F. nucleatum* abundance for adjacent normal tissues (right) and OSCC cancerous tissues (left) is plotted. A total of 70 matched OSCC tissue pairs were tested. Each symbol represents data from one sample (OSCC cancerous tissue and adjacent normal tissue) (one-way-ANOVA), P = 0.0006. (B–D) *F. nucleatum* abundance for OSCC tissues with or without cervical lymph node metastasis (B), at high, middle and low pathological stages (C), as well as with flange, spike and skipping invasive phenotypes (D). (one-way-ANOVA), (B), P = 0.0231; (C), ANOVA P = 5.0E-16; (D), ANOVA P = 7.9E-05. (E) Representative images of H&E staining for tissue structure (up) and *F. nucleatum* spatial distribution by FISH staining (down) from clinical samples of OSCC lesions with flange, spike and skipping invasive phenotypes, respectively. Black and white curves indicate the borders between tumor tissues and adjacent normal tissues. (F) Representative data of xenograft tumors in C3H mice bearing SCC-7 cells in different groups.

(1 mM) under ultrasonic oscillation discussed below. Lysed solutions were then centrifuged at 700 g for the eradication of debris. Subsequent centrifugation was applied at 14000 g for 30 min, and cytosolic proteins were left in the supernatant. For acquisition of membrane proteins, the above precipitations were centrifuged again at 14000 g for 10 s, followed by the addition of Reagent B and subsequent vortex for 5 s. After repeated operations 2–3 times, membrane proteins could be acquired from the supernatant.

Western blot analysis

Experimental cell samples were washed with pre-cold PBS three times and subsequently lysed with RIPA (Beyotime) buffer supplemented with 2 μg/mL protease inhibitors (Biosharp) inside an ice bath for 20 min. Ultrasonic oscillation treatment at the frequency of 2s pulse-on/1s pulse-off was applied 10 times to acquire protein samples from cell-lysed products. Each sample (30 μg) was electrophoresed on 8% or 10% SDS-PAGE gels at 85V for 2.5 h and followed by transferring from SDS-PAGE gels to polyvinylidene difluoride (PVDF) membranes at 300 mA for 90 min. PVDF membranes loaded with proteins were then blocked with 5% BSA for 1 h and subsequently incubated with primary antibodies targeted at specific proteins overnight. After incubation with HRP-conjugated secondary antibodies for 1–2 h, protein blots were captured visually by a chemiluminescent (ECL) detecting system.

Immunofluorescent staining

After experimental operations on seeded cells, 4% formaldehyde was applied for fixation, and 0.5% Triton X-100 was selected for subsequent permeabilization. 5% BSA buffer was used for 1–2 h for efficient background blocking. Incubation of primary antibodies and cells overnight was implemented to bind target proteins. Anti-rabbit Alexa Fluor Cy3, 488, 594 (Invitrogen) secondary antibodies were applied for fluorescent marking of specific proteins at room temperature, followed by DAPI staining for labeling the cell nucleus.

Quantitative reverse transcription qRT-PCR analysis

Trizol (Takara, Tokyo, Japan) was applied to extract total RNA according to the manufacturer's protocols. cDNA was produced from mRNA with oligo dT primers and reverse transcriptase (Takara). Real-time RT–PCR was performed with SYBR Green PCR kit and real-time PCR system (Applied Biosystems, Carlsbad, CA, USA). Relative mRNA expression was normalized by GAPDH using the $2^{-\triangle\triangle Ct}$ scheme.

DNA extraction and quantification of bacteria by qPCR

Total DNA extraction was carried out on OSCC clinical samples freshly stored in liquid nitrogen by DNA extraction kit (Tiangen, China) following the manufacturer's instructions. 16S-rDNA amplification was performed using *F. nucleatum* specific primers (Forward: 5′-CAACCATTACTTTAACTCTACCATGTTCA 3′, Reverse: 5′ ATTGACTTTACTGAGGGAGATTATGTA AAAATC 3′). This amplification process was operated in a 10 μL reaction system containing a 1 ng DNA template. The reaction process was run as follows: 50 °C for 2 min, 95 °C for 10 min, running of 40 cycles for 15 s at 95 °C and 60 °C for 1 min. The cycle threshold (Ct) values were normalized according to the host DNA in each reaction with the primer for the housekeeper gene (*GAPDH*).

Flow cytometry analysis

For measurement of changes in the percentage of M2 macrophages, THP-1 cell lines were harvested after indirectly co-cultured with tumor cells under different conditions for 48 h. Cells were then washed with PBS for repeated times, blocked by 5% BSA and resuspended with 100 μL buffer mixed with 5 μL anti-body (Elabscience, E-AB-F1135E) for 30 min, and finally subjected to flow cytometry.

Quantification of glucose, pyruvate, lactic acid and citric acid

After experimental treatment operated on cells, cell culturing supernatant was collected and purified by 0.22 μm filters. The filtered liquid was then diluted with PBS to a proper concentration for subsequent measurement. Glucose assay kit (Nanjing Jiancheng, F006-1-1), Pyruvate assay kit (Nanjing Jiancheng, A081-1-1), Lactic acid assay kit (Nanjing Jiancheng, A019-2-1) and Citric acid assay kit (Nanjing Jiancheng, A128-1-1) were applied for quantification of glucose, pyruvate, lactic acid and citric acid following the recommended instructions.

Quantification of ATP production, SDH and MDH activity

Cells prepared for detection were first collected and lysed by RIPA in an ice bath. A centrifuged at 12000 g for 5 min was carried out for purification, following the

Local injection of *F. nucleatum* was applied to establish the *F. nucleatum*-associated tumor model. (G and H) Statistical analysis of mouse tumor weights (I) and volumes (J) in different groups. n = 5/group (two-tailed t test), Weight, *P* = 3.5E-05; Volume, *P* = 0.0052. (I) Representative FISH images of clinical OSCC samples using *F. nucleatum*-specific 16S rDNA-directed probe (left) and fluorescent images stained with 488-anti-SOX2, 488-anti-N-cad and 488-anti-ZEB1 (right) for measurement of tumor invasive levels by successive sections. (J) Representative fluorescent images of xenograft tumor samples with or without *F. nucleatum* infection stained with SOX2 (green), N-cad (green) and DAPI (blue).

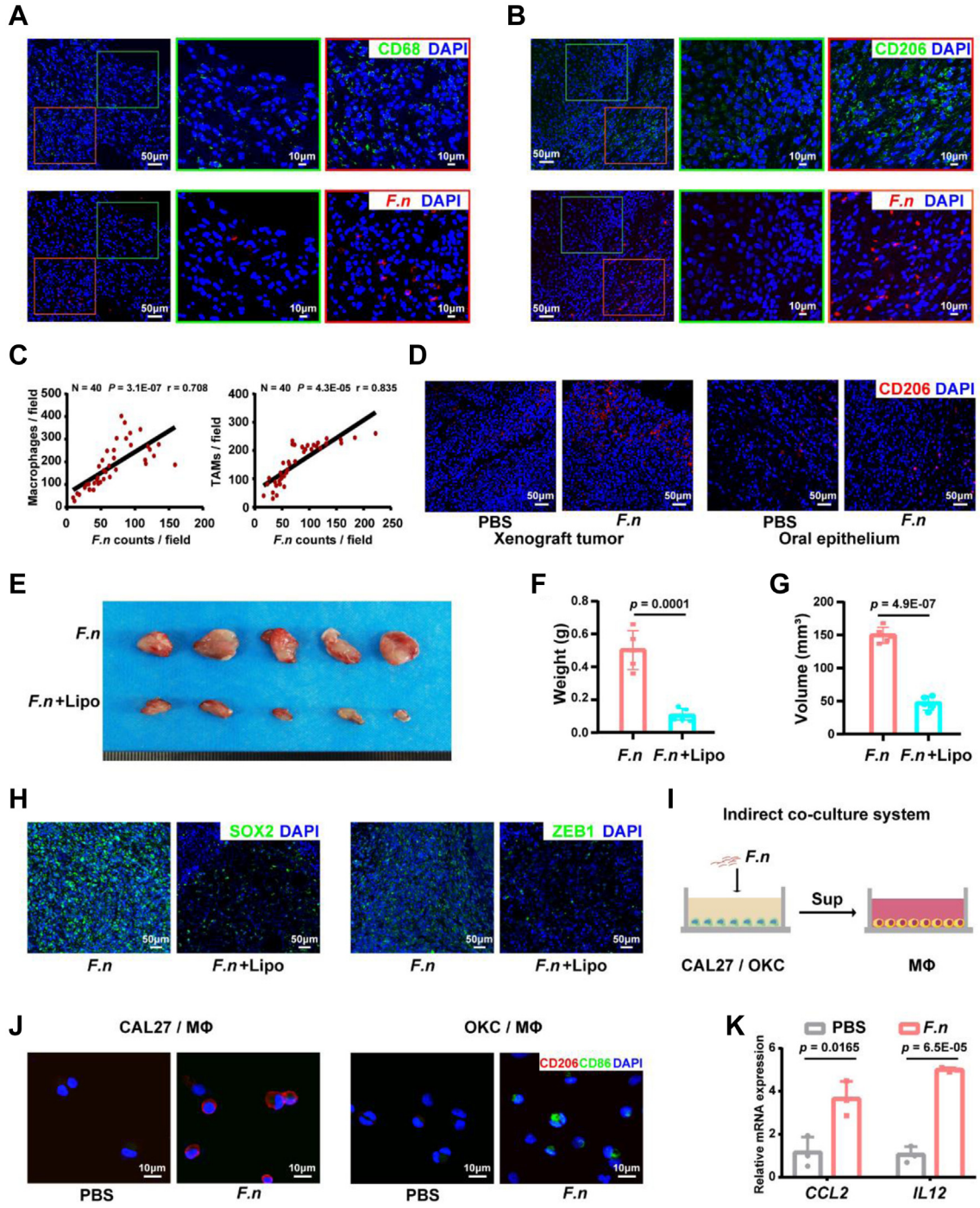

***Fig. 2:* Colonized *F. nucleatum* drives M2-like tumor-associated macrophages formation.** (A and B) Representative fluorescent images of *F. nucleatum* spatial distribution, total macrophages and TAMs enrichment status in successive sections from clinical OSCC samples. Cy3-labeled *F. nucleatum*-specific probe was used for the detection of *F. nucleatum*. 488-anti-CD68 and 488-anti-CD206 were applied to visualize total macrophages and TAMs, respectively. A total of 40 paired successive sections on OSCC primary locus were tested to explore the relationship between *F. nucleatum* colonization and macrophage accumulation. (C) The Pearson linear correlation analysis was conducted based on *F. nucleatum* counts, total macrophages and TAMs in OSCC. (D) Representative fluorescent images of xenograft tumor samples (left) or normal oral epithelial samples (right) from C3H mice with or without *F. nucleatum* colonization stained with Cy3-anti-CD206 for identification of TAMs. (E) Representative data of xenograft tumors in C3H mice bearing SCC-7 cells in different groups. Local injection of *F. nucleatum* was used for *in vivo F. nucleatum*-associated tumor model. Injection of clodronate liposomes was applied for the eradication of local macrophages. (F and G)

acquisition of supernatant. ATP assay kit (Beyotime, S0026), succinodehydrogenase (SDH) assay kit (Nanjing Jiancheng, A022-1-1) and malic dehydrogenase (MDH) assay kit (Nanjing Jiancheng, A021-1-1) were applied to quantify cell ATP production, SDH and MDH activity respectively based on the recommended instructions.

Microscopy and visualization of *F. nucleatum* by fluorescence in situ hybridization (FISH)

4% PFA fixed oral cancer samples from clinical patients, and animal xenograft models were prepared into tissue slides (3–5 μm). The fluorescence in situ hybridization (FISH) experiment was performed by applying probes specific to *F. nucleatum* ribosomal 16S-rRNA gene sequences on tissue sections. Briefly, tissue sections were incubated with 8 mg/mL *F. nucleatum* 16S rRNA-specific oligonucleotide pb-2634 5'- CTTGTAGTTCCGCYTACCTC-3' labeled with Cy3 in the hybridization solution, slides were then counterstained with DAPI for visualization of the cell nucleus. Blocking buffer, hybridization buffer, and wash buffer contained protective RNA to protect bacterial RNA from degradation.

Microscopy of fluorescent images

The fluorescent images were visualized and captured on a confocal microscope (Nikon A1-Si) with NIS software for acquisition. Fluorescence intensities reflecting the distribution of electroporated cells within regions of interest were converted into gray values and measured using ImageJ software.

Ethics

This study was approved by the Institutional Research Ethics Committee of Tongji Medical College (Wuhan, China). The ethical approval numbers were S1117 and S2931 for clinical and animal experiments respectively.

All animal experiments were performed with the consent of the Institutional Animal Care and Use Committee of Tongji Medical College, and the associated checklist according to the ARRIVE guidelines has also been offered in the Supplementary sections.

Statistics

Statistical analysis was performed in this study using the software Graphpad Prism 7.00 (San Diego, CA, USA). Shapiro–Wilk test was conducted on the experimental data collected in this study to ensure whether they are in accordance with the normal distribution to determine their further statistical comparison, and all data sets in this article passed the normality distribution test. Paired or unpaired Student's t-test methods were applied for comparison between two groups, and one-way ANOVA test was performed to compare the differences among multiple groups, followed by Tukey post-hoc tests or repeated measure ANOVA, as well as Bonferroni post-hoc tests for correction.

Based on the normal distribution and paired clinical data volume, relationship between macrophage infiltration and *F. nucleatum* amounts were measured by Pearson correlation analysis.

For clinical sample size, calculation for this cross-sectional study was performed using the function Confidence Intervals for One Proportion in software PASS v15.0.[24] Pre-experiments estimated that the positive rate of *F. nucleatum* in OSCC tissues was at 72%, and the estimated positive rate was hypothesized as 72%. An incidence of <12% was considered clinically irrelevant, and formula N' = N/(1 – DR) was applied for sample size calculation.[25] Results showed that by including at least 75 patients diagnosed with OSCC and assuming a 72% positive rate of *F. nucleatum*, an actual <10% positive rate could be rejected with 90% power and 95% (two-sided) confidence at the 5% significance.

For animal sample size, independent T test method was selected to evaluate experimental sample size. Based on the formula $t = \frac{\overline{X}-\mu_0}{S/\sqrt{n}}$, $\overline{X}$ and S were set as the mean xenograft tumor weight (0.68 g) and its estimated standard deviation (0.1 g) by our pre-experiment for this study, μ0 was regarded as the mean weight of xenograft tumor (0.25 g) based on previous study in our laboratory. To acquire the powerful results of statistical analysis ($P < 0.05$), $t > t0.05/2$, $n - 1$ should be satisfied. Results showed that only when $n \geq 3$ could the standard for powerful analysis of xenograft tumor analysis get satisfied, which was just consistent with previous studies.[4]

Simple random sampling method was used for randomization of samples applied in this research. Briefly, each of the mice was randomly set a number for drawing lots to ensure that these selected mice were given equal opportunity to be divided into each experimental group.

Statistical analysis of mouse tumor weights (I) and volumes (J) in different groups. n = 5/group (two-tailed t test), Weight, $P = 0.0001$; Volume, $P = 4.9E-07$. (H) The fluorescent assay showed a significant reversal of *F. nucleatum*-induced EMT markers (SOX2 and ZEB1) upregulation by eradicating local macrophages using clodronate liposomes. (I) schematic graph of indirect co-culture system including two crucial steps: extraction of oral tumor/epithelial cell culturing supernatant with or without *F. nucleatum* infection, and stimulation of M0 macrophages by extracted cell supernatant. (J and K) Assessment of macrophage polarization status in the indirect co-culture system mentioned above by immunofluorescent assay for CD86+ (green) M1-like macrophages and CD206+ (red) M2-like macrophages derived from M0 macrophages (J) as well as measuring mRNA expression of M2 markers (*CCL2* and *IL12*) in macrophages (K) indirectly co-cultured with oral tumor/epithelial cells with or without *F. nucleatum* infection (two-tailed t test), *CCL2*, $P = 0.0165$; *IL12*, $P = 6.5E-05$.

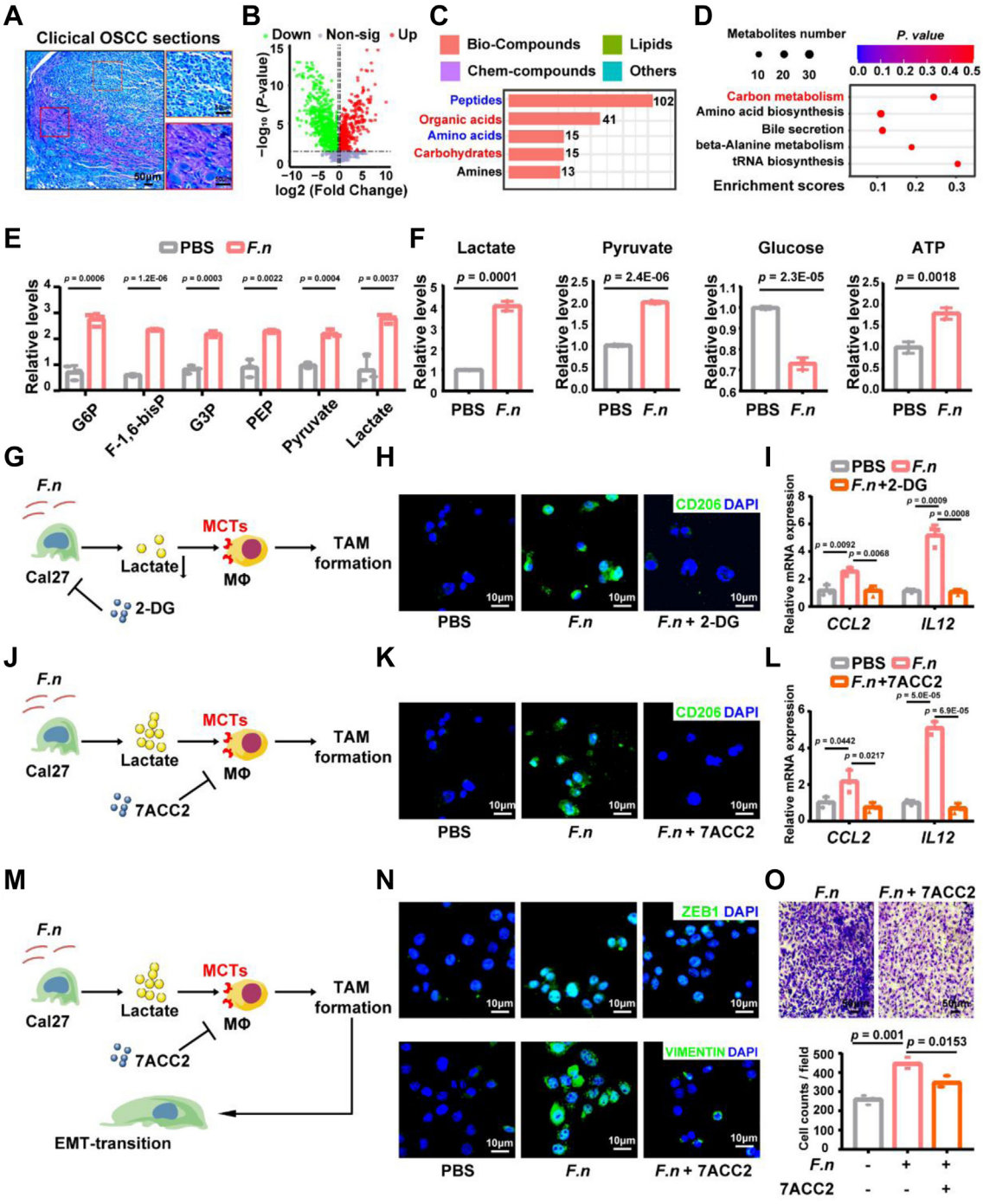

***Fig. 3: F. nucleatum*-induced lactate production of OSCC cells is required for M2-like tumor-associated macrophages formation.** (A) Representative Giemsa staining images of OSCC invasive margins. The red square indicates the acidic border between tumor tissue and adjacent normal tissue, and the orange square indicates the non-acidic central regions. (B) Volcano plot for metabolite changes in filtered cell culturing supernatant with or without *F. nucleatum* infection. The red and green symbols indicate significantly upregulated and downregulated metabolites between the two groups. (C) Metabolic classification analysis of the top 5 metabolic terms based on differential metabolites in different groups (ranked by the number of enriched metabolites). (D) Pathway enrichment analysis of the top 5 metabolic pathways based on differential metabolites between the above two groups. (E) Alteration of intermediate metabolites of glycolysis in CAL27 culturing supernatant with or without infection of *F. nucleatum* (two-tailed t test), G6P, $P = 0.0006$; F-1,6-bisP, $P = 1.2E-06$; G3P, $P = 0.0003$; PEP, $P = 0.0022$; Pyruvate, $P = 0.0004$; Lactate, $P = 0.0037$. (F) Infection of *F. nucleatum* significantly enhanced the production of lactate, pyruvate, glucose

For clinical and animal experiments, single-blind method was applied in this research.

For inclusion of clinical participants, patients diagnosed with OSCC using pathological and clinical evidence, and could offer complete clinical samples and information were recruited in our study.

For exclusion of animal samples, any mice which failed to establish xenograft tumor model, or died during the experimental period owing to other reasons were excluded from our study.

Data were shown as mean ± Standard Error of Mean (SEM). A *P*-value less than 0.05 was regarded as statistically significant. Precise *P* values were recorded in the Figures and Figure legends section.

Role of funding source

The funding sources for this project played no role in the study design, data collection, analysis, interpretation, writing or editing of the manuscript.

Results

F. nucleatum aggregates at the invasive margin of OSCC and correlates with tumor invasion

To define the interrelationship between *F. nucleatum* colonization and OSCC progression, we analyzed the 16S rRNA sequencing data from the two representative cohorts (PRJNA415963, SRP097643).[26,27] The results showed that *Fusobacterium* was one of the most prevalent pathogens colonized in OSCC tissues (Fig. S1A and S1B). The subspecies *F. nucleatum* was observed in 75.7% of OSCC samples, and *F. nucleatum* prevalence was significantly lower by 2.25-fold in adjacent normal tissues (Fig. 1A and Fig. S1C). Notably, more *F. nucleatum* was detected in the samples with lower histological grade or lymphatic metastasis, especially in the samples of malignant invasive growth, including spike and skipping (Fig. 1B–D). Together, these results demonstrated an apparent correlation between *F. nucleatum* colonization and OSCC progression.

To determine the localization of *F. nucleatum* within OSCC tissues, we applied a specific probe for a fluorescent in situ hybridization assay. We found that *F. nucleatum* often aggregated in the invasive margins of all types of OSCC (Fig. 1E). In the OSCC xenograft tumor formation experiments, we observed about 2.0-fold tumor weight and 1.7-fold tumor volume in the group with local injection of *F. nucleatum* compared with the tumors without *F. nucleatum* inoculation (Fig. 1F–H and Fig. S2A and S2B). By immunofluorescent staining in the successive sections of clinical OSCC samples, we verified that a cohort of epithelial–mesenchymal transition (EMT) biomarkers, including sex-determining region Y-box 2 (SOX2), N-cadherin and zinc finger E-box-binding homeobox 1 (ZEB1), were significantly increased in the *F. nucleatum*-enriched regions (Fig. 1I). Taken together, these findings suggested that OSCC-resident *F. nucleatum* could facilitate epithelial–mesenchymal transition (Fig. 1J and Fig. S2C), corroborating the correlation between *F. nucleatum* and OSCC invasion.

Colonized *F. nucleatum* drives M2-like tumor-associated macrophages formation

M2-like tumor-associated macrophages (TAMs) are capable of promoting tumor invasion.[21,22] Of note, *F. nucleatum* infection has been shown to induce macrophage infiltration.[20] Thus, to define whether *F. nucleatum* promotes OSCC invasion via M2-like TAMs, we first assayed the immune response caused by *F. nucleatum* colonization. In the successive section of OSCC clinical samples, we noticed that macrophages presented a significant increase upon *F. nucleatum* colonization (Fig. 2A). Specifically, CD206(+) M2-like macrophages showed a predominant overlap with *F. nucleatum* in the unit view (Fig. 2B and C). After injecting *F. nucleatum* into OSCC xenograft tumor or oral epithelium, CD206(+) M2-like macrophages were only abundantly presented in the tumor microenvironment rather than in the normal tissue (Fig. 2D, Fig. S3A and S3B), suggesting that *F. nucleatum* inoculation is capable of promoting CD206(+) M2-like TAMs formation. Consistently, tumor progression was reversed by eliminating macrophages using clodronate liposomes by 0.4 ± 0.05 g in weight and 102.8 ± 7.08 mm^3 in volume (Fig. 2E–G and Fig. S3C and S3D). The expressions of the EMT biomarkers SOX2 and ZEB1 were reduced (Fig. 2H). Furthermore, our *in vitro* assays

consumption, and production of ATP in CAL27 cells. (two-tailed t test), Lactate, *P* = 0.0001; Pyruvate, *P* = 2.4E-06; Glucose consumption, *P* = 2.3E-05; ATP production, *P* = 0.0018. (G) Schematic graph of indirect co-culture system includes two crucial steps: extraction of CAL27 cell culturing supernatant with or without *F. nucleatum* infection, and stimulation of M0 macrophages by extracted cell supernatant with or without addition of 7ACC2 (10 μM) for inhibition of lactate adsorption. (H and I) Assessment of macrophage polarization status by measuring mRNA expression of M2 markers (*CCL2* and *IL12*) (I) as well as immunofluorescent assay of CD206 (J) in CAL27 cells treated with DMSO, *F. nucleatum* suspension or 7ACC2. (one-way-ANOVA), *CCL2*, ANOVA *P* = 0.0048; *IL12*, ANOVA *P* = 5.3E-05. (J) Schematic graph of indirect co-culture system including two crucial steps: extraction of oral tumor cell culturing supernatant with or without *F. nucleatum* infection plus 2-DG (20 mM) for inhibition of glycolysis, and stimulation of M0 macrophages by extracted cell supernatant. (K and L) Assessment of macrophage polarization status by measuring mRNA expression of M2 markers (*IL10* and *IL12*) (I) as well as immunofluorescent assay of CD206 (J) in CAL27 cells treated with DMSO, *F. nucleatum* suspension or 2-DG. (one-way-ANOVA), *CCL2*, ANOVA *P* = 0.0141; *IL12*, ANOVA *P* = 1.7E-06. (M) Schematic graph depicting indirect co-culture system with *F. nucleatum*-mediated TAM failed to promote tumor invasive behavior by inhibiting lactate adsorption of macrophages using 7ACC2. (N and O) Fluorescence assay of CAL27 cells for expression levels of ZEB1 and VIMENTIN (left) and Transwell assay depicting OSCC invasive potential under the above conditions. (one-way-ANOVA), ANOVA *P* = 0.0005.

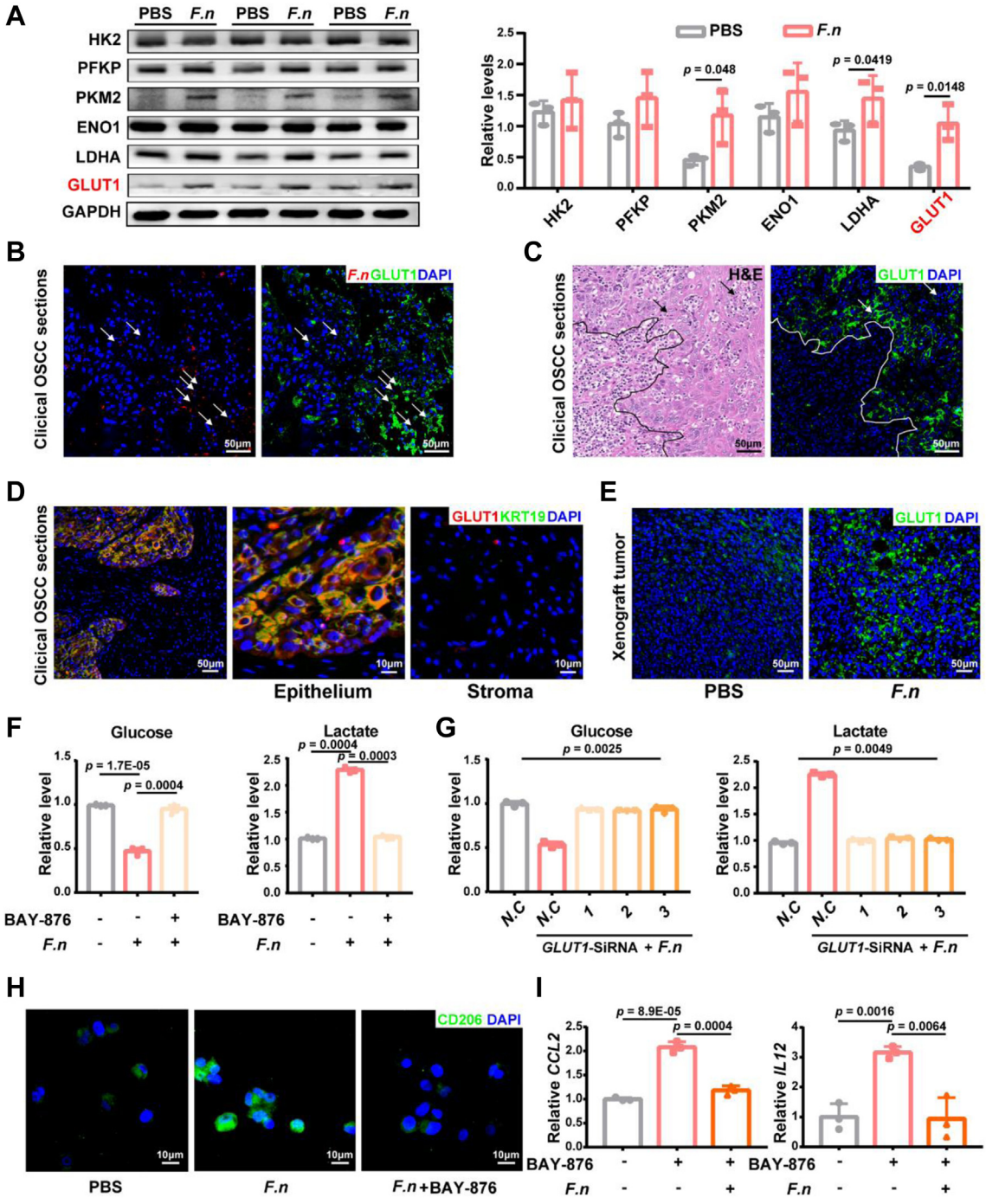

***Fig. 4: F. nucleatum*-induced accumulation of GLUT1 increases lactate production of OSCC cells.** (A) Western blot analysis of glycolysis-related rate-limiting components (HK2, PFKP, PKM2, ENO1, LDHA, GLUT1) and GAPDH (for loading controls) in CAL27 cells co-cultured with or without *F. nucleatum*. All experiments were performed repeatedly three times. (two-tailed t test), PKM2, *P* = 0.048; LDHA, *P* = 0.0419; GLUT1, *P* = 0.0148. (B) Representative fluorescent images of successive sections from OSCC tissues for localization of *F. nucleatum* (red) and GLUT1 (green). (C) Representative images of GLUT1 (green) expression pattern in OSCC. (D) Clinical OSCC sections stained with 488-anti-KRT19 (green) and Cy3-anti-GLUT1 (red). High expression levels of GLUT1 could be detected mainly in KRT19+ tumor cells. (E) Representative images of xenograft tumor sections for measurement of GLUT1 expression (green) after injection of *F. nucleatum* suspension or PBS vehicle. (F and G) Glucose uptake and lactate production in CAL27 cells treated with *F. nucleatum* infection, BAY-876 (50 nM) or GLUT1 knockdown operations. (one-way-ANOVA), (F), Glucose, ANOVA *P* = 1.7E-06; Lactate, ANOVA *P* = 0.0142. (G), Glucose, ANOVA *P* = 0.0025;

demonstrated that *F. nucleatum*-induced CD206(+) M2-like polarization mainly depended on the tumor cells co-cultured system (*CCL2*, 2.5 ± 0.62 fold increase; *IL12*, 3.9 ± 0.22 fold increase. Fig. 2I–K, and Fig. S3E–S3G). Together, these data suggested that *F. nucleatum* within the tumor microenvironment could promote CD206(+) M2-like TAMs formation, which is potentially vital for *F. nucleatum*-induced OSCC invasion.

F. nucleatum-induced lactate production of OSCC cells is required for M2-like tumor-associated macrophages formation

To dissect the underlying mechanisms that *F. nucleatum* encourages M2-like TAMs formation, we assayed a series of tumor pathophysiological processes. Interestingly, extracellular acidification was significant in the *F. nucleatum*-aggregated OSCC invasive margins and the *in vitro* co-cultured system (Fig. 3A and Fig. S4A). Accordingly, we performed metabonomic analysis to acquire the acidic metabolites profile of *F. nucleatum*-exposed OSCC cells (Fig. 3B and Fig. S4B). Differential metabolite pathway enrichment analysis revealed significantly activated carbon metabolism (G6P, 2.04 ± 0.21 fold increase; F-1,6-bisP, 1.75 ± 0.03 fold increase; G3P, 1.36 ± 0.11 fold increase; PEP, 1.41 ± 0.20 fold increase; Pyruvate, 1.22 ± 0.11 fold increase; Lactate, 1.99 ± 0.32 fold increase. Fig. 3C–E). Glucose consumption, lactate, pyruvate and ATP synthesis rose proportionately (Lactate, 3.06 ± 0.13 fold increase; Pyruvate, 98.92% ± 2.48% increase; Glucose, 26.75% ± 1.73% increase; ATP, 79.51% ± 10.84% increase. Fig. 3F).

To explore whether lactate deposition could promote M2-like TAMs formation in the tumor microenvironment, we added the lactate metabolism inhibitor 2-DG to suppress lactate deposition in the OSCC cells co-cultured system. The data showed that 2-DG reversed *F. nucleatum*-mediated M2-like polarization of macrophages (Fig. 3G–I, Fig. S4C and 4D). Likewise, inhibition of macrophages lactate ingestion by 7ACC2 suppressed M2-like polarization (Fig. 3J–L and Fig. S4C–S4F). Moreover, macrophages without lactate ingestion could not promote EMT progression of OSCC cells, thereby reversing *F. nucleatum*-mediated tumor cell invasion (Fig. 3M–O and Fig. S4G–S4I). Collectively, these findings supported that *F. nucleatum* promotes OSCC cell glycolysis and lactate production, which in turn increases extracellular acidification and M2-like TAMs formation.

F. nucleatum-induced accumulation of GLUT1 increases lactate production of OSCC cells

To elucidate how *F. nucleatum* infection increases lactate production of OSCC cells, we scrutinized the expressions of glucose transporters and the glycolysis rate-limiting enzymes in *F. nucleatum*-exposed OSCC cells. Remarkably, GLUT1, highly expressed in OSCC tissues, was upregulated around 3-fold under *F. nucleatum* stimulation (Fig. 4A, and Fig. S5A and S5B). Consistently, functional enrichment analysis based on the above metabonomic data of *F. nucleatum*-exposed OSCC cells indicated that the membrane transport associated with GLUT1 was the top term (Fig. S5C).

Then, we performed immunofluorescent staining in the successive sections of clinical OSCC samples. We noticed that GLUT1 was mainly enriched in OSCC invasive margins and presented a predominant overlap with *F. nucleatum* colonization (Fig. 4B and C). Keratin-19 (KRT19) has been suggested to play a key role in tumorigenic transformation.[28] Inside the clinical OSCC tissues, KRT19-positive tumor cells showed a higher GLUT1 level than the stroma cells (Fig. 4D). Likewise, *F. nucleatum* inoculation resulted in significant GLUT1 upregulation in the OSCC xenograft tumor formation experiments (Fig. 4E). Taken together, our results suggested that *F. nucleatum*-induced lactate production could correlate with the upregulation of GLUT1 in OSCC cells.

To consolidate the implication of *F. nucleatum*-induced GLUT1 upregulation in lactate deposition, we pretreated OSCC cells with the GLUT1 selective inhibitor BAY-876 to restrict glucose transport. As expected, *F. nucleatum* failed to increase the lactate production in BAY-876-treated OSCC cells (Fig. 4F). A similar effect was obtained by knockdown of GLUT1 with specific siRNA (Fig. 4G and Fig. S5D). Accordingly, destabilization of GLUT1 by Bafilomycin A1 downregulated *F. nucleatum*-mediated lactate deposition (Fig. S5G). In comparison, tricarboxylic acid cycle indicated only slight changes along with GLUT1 variations (Fig. S6). Then, we examined the M2-like polarization of macrophages in the experimental scenario described above. Consistent with limited lactate production, inhibition of the function of GLUT1 in OSCC cells by BAY-876 treatment or *Glut*-siRNA significantly reversed *F. nucleatum*-mediated M2-like polarization of macrophages (Fig. 4H and I, and Fig. S5E and S5F). Together, our data suggested that *F. nucleatum*-induced GLUT1 upregulation in OSCC cells accounts for the increased deposition of lactate.

F. nucleatum-induced TBC1D5 downregulation promotes GLUT1 localization on the cell surface

To delineate the cause of *F. nucleatum*-mediated GLUT1 upregulation, we first evaluated the transcription of *GLUT1* in *F. nucleatum*-incubated OSCC cells. The qRT-PCR assays showed that the transcription of *GLUT1* had no significant change in OSCC cells pretreated with

Lactate, ANOVA $P = 0.0049$. (H and I) Evaluation of macrophage polarization status by confocal fluorescence assay for CD206 (H) and mRNA expression levels of *CCL2* and *IL-12* (I). Macrophages were indirectly co-cultured with CAL27 cells treated by PBS, *F. nucleatum* infection or BAY-876. (one-way-ANOVA), *CCL2*, ANOVA $P = 0.0001$; *IL12*, ANOVA $P = 0.0216$.

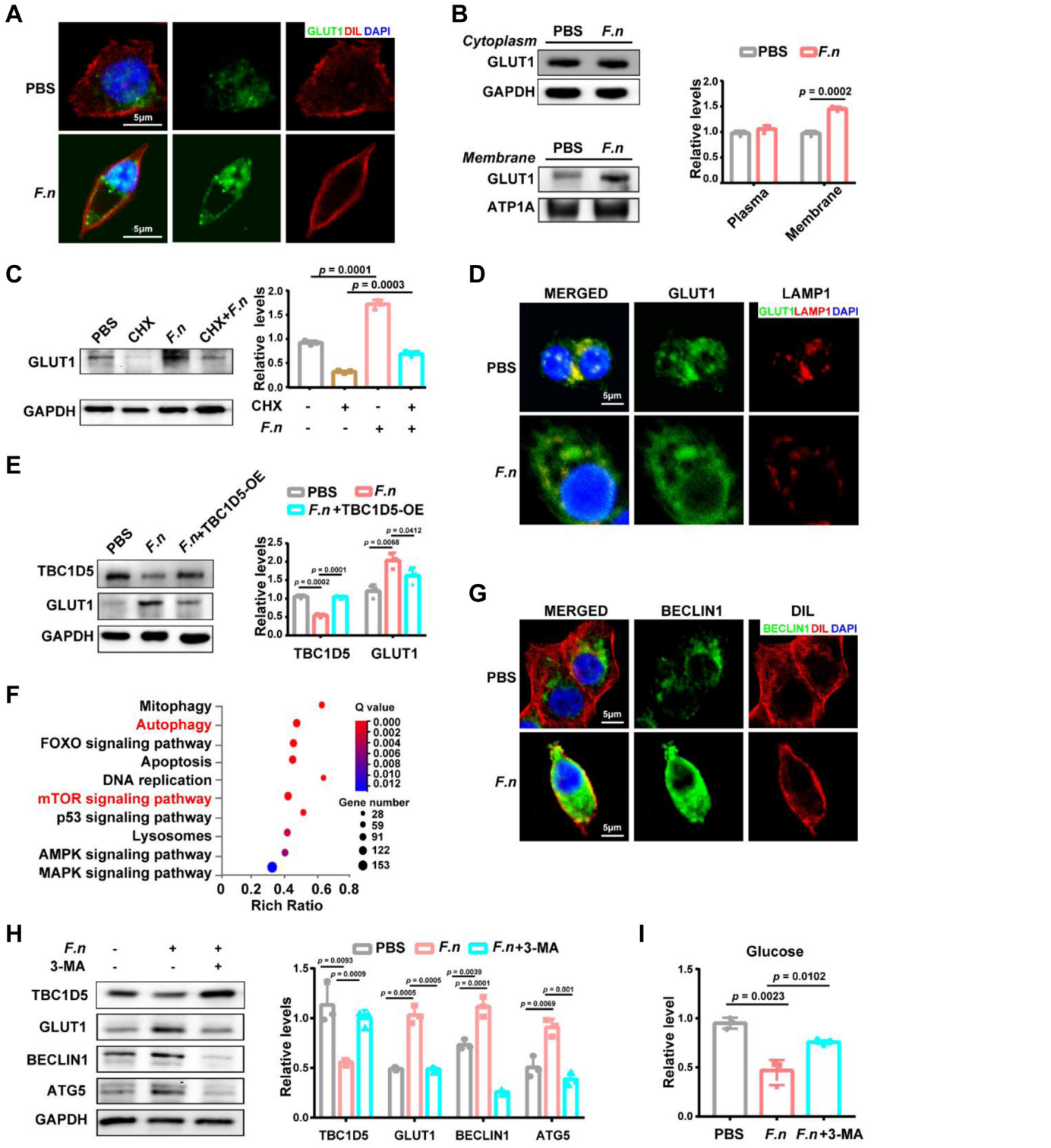

***Fig. 5: F. nucleatum* promotes GLUT1 localization on the cell surface through autophagy-dependent TBC1D5 decrease.** (A) Representative confocal images of GLUT1 (green) and DIL-labelled cellular membrane (red) in CAL27 cells with or without *F. nucleatum* co-culture. (B) Western blot analysis of GLUT1 in the cytoplasm and cellular membrane of CAL27 cells with or without *F. nucleatum* infection. GAPDH was applied as the loading control for cytoplasm protein, and ATP1A was used as the loading control for membrane protein (two-tailed t test), P = 0.0002. (C)

different multiplicity of infection (MOI) of *F. nucleatum* (Fig. S7A). However, immunofluorescence staining showed more GLUT1 proteins on the cell surface of *F. nucleatum*-incubated cells than those in the control cells (Fig. 5A). We examined membrane-bound and cytosolic protein levels to determine whether this cell surface presence signified increased protein levels or only a change in protein distribution. Western blotting assays showed that the membrane-associated GLUT1 was significantly elevated by 47.99% ± 3.84%. In contrast, cytoplasm GLUT1 exhibited a slight increase (Fig. 5B), suggesting that both protein level and cell surface localization of GLUT1 were increased.

To determine whether upregulation of protein translation is responsible for the above phenotypes, we utilized cyclohexane (CHX) pretreatment for protein translation inhibition. Nevertheless, CHX application could not reverse *F. nucleatum*-mediated GLUT1 upregulation in a certain period (Fig. 5C), suggesting that *F. nucleatum*-mediated GLUT1 accumulation may result from protein degradation inhibition. To test this speculation, we compared the intracellular distribution of GLUT1 with that of lysosome-associated membrane glycoprotein 1 (LAMP1) in *F. nucleatum*-exposed OSCC cells. Immunofluorescence staining showed reduced localization of GLUT1 on LAMP1-positive structures in *F. nucleatum*-exposed cells (Fig. 5D), supporting that *F. nucleatum* may inhibit GLUT1 lysosomal degradation. In addition, ubiquitination-associated protein degradation pathway showed no significant relationship with *F. nucleatum*-mediated GLUT1 stabilization (Fig. S7D–S7G).

A previous study showed that the inhibitory interaction of TBC1 domain family member 5 (TBC1D5) with retromer could lead to GLUT1 mis-sorting into endolysosomal compartments.[29] Notably, we observed a downregulation of TBC1D5 in *F. nucleatum*-incubated OSCC cells (Fig. 5E). TBC1D5 overexpression offset *F. nucleatum*-induced GLUT1 upregulation in OSCC cells (Fig. 5E). Together, these observations suggested that *F. nucleatum* promotes cell surface presence of GLUT1 via downregulating TBC1D5.

F. nucleatum-induced autophagy leads to TBC1D5 downregulation

To define the underlying mechanism of TBC1D5 downregulation, we first performed genome-wide RNA sequencing to acquire the transcriptional profile of *F. nucleatum*-exposed OSCC cells. Functional enrichment analysis revealed that autophagy and autophagy-related kinase signaling, including Serine/threonine-protein kinase mTOR, 5′-AMP-activated protein kinase catalytic subunit alpha-2 (AMPK) and Mitogen-activated protein kinase (MAPK), were enriched in OSCC cells infected with *F. nucleatum* (Fig. 5F).

Then, using autophagy marker beclin-1 (BECLIN1) and autophagy protein 5 (ATG5), our immunofluorescence staining and western blotting assays sustained that *F. nucleatum* could boost autophagy in OSCC cells (Fig. 5G and Fig. S7B). Moreover, activation of autophagy with rapamycin reduced the level of TBC1D5 (Fig. S7C), suggesting that *F. nucleatum*-induced autophagy could mediate TBC1D5 downregulation. In agreement with this speculation, the application of autophagy inhibitor 3-MA reversed *F. nucleatum*-induced TBC1D5 decrease, GLUT1 increase, and glucose uptake in OSCC cells (Fig. 5H and I, and Fig. S7H). Similarly, siRNA-mediated knockdown of *ATG5* reversed the effects of *F. nucleatum* infection (Fig. S7I–S7K). Taken together, these findings demonstrated that *F. nucleatum* could activate autophagy to reduce the level of TBC1D5. Of note, these results are consistent with the previous report that the autophagic compartment is capable of binding and sequestering TBC1D5 away from the retromer, thus promoting GLUT1 plasma membrane translocation.[29]

F. nucleatum binds to GalNAc on OSCC cell surface to induce cell autophagy

Thus far, our results suggested that *F. nucleatum* inoculation activates OSCC cell autophagy, which facilitates GLUT1 translocation to the plasma membrane. To identify the membrane targets that mediate cell surface adhesion of *F. nucleatum*, we scrutinized the previously reported bacterial adhesion mediators, including Toll-like receptor 4 (TLR4), E-cadherin and *N*-acetylgalactosamine (GalNAc).[9,17,30] We noticed that GalNAc marked by FITC-labeled peanut agglutinin (PNA) was highly expressed in KRT19(+) tumor cells and *F. nucleatum* enrichment area (Fig. 6A and B). The adhesion of *F. nucleatum* on OSCC cell surface was inhibited by blocking GalNAc with PNA, while

Western blot analysis of GLUT1 in CAL27 cells with or without *F. nucleatum* infection after pretreatment of CHX for 6 h at the proper concentration of 50 μg/mL. GAPDH was applied as the loading control. (one-way-ANOVA), ANOVA P = 7.4E-09. (D) Fluorescence assay for colocalization of GLUT1 (green) and LAMP1 (red) in CAL27 cells with or without *F. nucleatum* infection. (E) Western blot analysis of TBC1D5 and GLUT1 in CAL27 and CAL27/TBC1D5 treated by *F. nucleatum* infection or not. (one-way-ANOVA), TBC1D5, ANOVA P = 1.2E-05; GLUT1, ANOVA P = 0.0076. (F) The functional enrichment analysis of differentially expressed genes between CAL27 cells with or without *F. nucleatum* infection. (G) Confocal images of BECLIN1 (green) and DIL-labelled cellular membrane (red) in CAL27 cells with or without *F. nucleatum* infection. (H) Indicated proteins were detected by Western blot in CAL27 cells. The cells were co-cultured with *F. nucleatum* or treated by 3-MA (12 mM) for inhibition of autophagy. (one-way-ANOVA), TBC1D5, ANOVA P = 0.0040; GLUT1, ANOVA P = 2.3E-05; BECLIN1, ANOVA P = 1.1E-05; ATG5, ANOVA P = 0.0008. (I) Measurement of glucose uptake in CAL27 cells treated by PBS, *F. nucleatum* suspension or 3-MA. (one-way-ANOVA), ANOVA P = 0.0005.

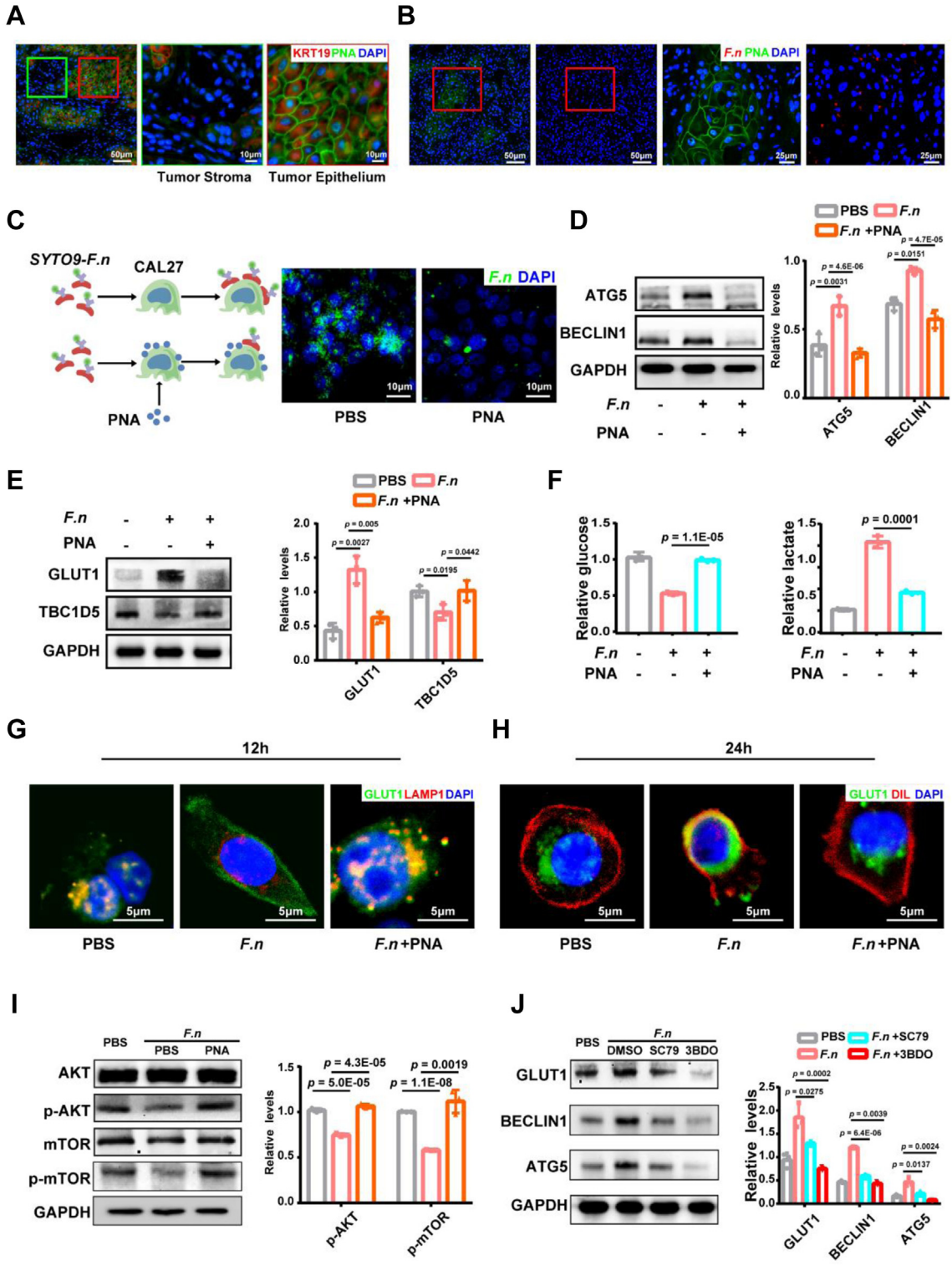

***Fig. 6: F. nucleatum* binds to GalNAc on OSCC cell surface to induce cell autophagy.** (A) Fluorescence assay of KRT19 (red) and GalNAc (green) in clinical OSCC sections. (B) Representative fluorescent images of *F. nucleatum* (red) and FITC-PNA (green) in clinical OSCC sections. (C) Confocal images of SYTO9-labelled *F. nucleatum* (green) in CAL27 cells treated by PBS or PNA solutions at the proper concentration of 80 μg/mL. (D and E) Western blot analysis of indicated proteins in CAL27 cells treated with PBS, *F. nucleatum* suspension or PNA solution (one-way-ANOVA), ATG5,

knockdown of E-cadherin by *CDH5*-siRNA or inhibition of TLR4 by TAK242 failed to do so (Fig. 6C, and Fig. S8A and S8B). Then, we observed that both autophagy activation and GLUT1 upregulation by *F. nucleatum* could be reversed with GalNAc blockade by PNA in OSCC cells rather than *CDH5*-siRNA and TAK242 (Fig. 6D and E, and Fig. S8C and S8D). Together, these results suggested that GalNAc is required for the OSCC cell adhesion of *F. nucleatum*.

We validated the efficacy of GalNAc by assaying additional phenotypes, including TBC1D5 down-regulation, GLUT1 upregulation, glucose uptake increase, and lactate production. As expected, these *F. nucleatum*-induced phenotypes were efficiently rescued by PNA treatment (Fig. 6D–F). Also, *F. nucleatum*-induced inhibition of GLUT1 transport into LAMP1(+) lysosomes was abolished by PNA addition (Fig. 6G and H).

AKT/mTOR is the classic intracellular signaling pathway associated with the membrane protein GalNAc.[31] Likewise, we observed that AKT/mTOR signaling pathway was significantly activated by *F. nucleatum*, and PNA reversed this effect (Fig. 6I). Blocking AKT/mTOR signaling with SC79 or 3BDO inhibited *F. nucleatum*-mediated cell autophagy activation and GLUT1 accumulation in OSCC cells (Fig. 6J). Altogether, our data indicated that *F. nucleatum* selectively binds to the membrane protein GalNAc on the OSCC cell surface to promote cell autophagy.

Double targeting at GalNAc and GLUT1 inhibits OSCC progression

Thus far, our results suggested that the GalNac-Autophagy-GLUT1-Lactate axis in OSCC cells orchestrates *F. nucleatum*-induced TAMs formation and tumor progression. To test whether xenograft tumor could be suppressed by targeting the two pivotal components (GalNAc and GLUT1) in tumor-bearing mice (Fig. 7A), we injected the *F. nucleatum*-incubated tumor-bearing mice with GalNAc inhibitor PNA and/or GLUT1 inhibitor BAY-876. Observation on the histological features of liver and kidney collected from treated mice indicated that the medical treatments possessed excellent biocompatibility (Fig. S9). The data showed that *F. nucleatum*-induced OSCC development was partially restrained by applying PNA or BAY-876 alone, validated by the reduction in the tumor weight and volume (Fig. 7B–D). Similarly, PNA or BAY-876 partially reduced the number of CD206(+) TAMs (Fig. 7E). *F. nucleatum*-recruited macrophages began to turn into CD86(+) anti-tumor M1-like macrophages (Fig. 7E). Notably, double targeting at GalNac and GLUT1 induced significant atrophy of OSCC xenografts and retrained *F. nucleatum*-associated OSCC immune landscape, which mediated a transfer of macrophages from M2-like to M1-like phenotype (Weight, 0.38 ± 0.04 g decrease; Volume, 96.27 ± 10.91 mm^3 decrease. Fig. 7B–E). We further found that the combined therapy effectively diminished *F. nucleatum*-induced EMT progression (Fig. 7F). Together, our data suggested that a combined therapeutic strategy by double targeting GalNAc and GLUT1 can efficiently overcome *F. nucleatum*-induced OSCC progression.

Discussion

Microbiota-host interactions have been documented to be involved in tumor progression.[32,33] The previous reports have unanimously shown that *F. nucleatum* is a well-known protumorigenic bacterium in multiple types of cancers, including colorectal, breast and esophagus tumors.[34–38] The amount of *F. nucleatum* within the tumor microenvironment is closely associated with malignant progression and shorter survival.[39,40] This study observed that *F. nucleatum* is characteristically accumulated at the periphery of clinical OSCC colonies. *F. nucleatum* leads to enhanced glycolytic metabolism and excessive extracellular lactate deposition in the tumor-stroma marginal regions. Extracellular acidification can induce transcriptome rewiring of cancer cells to acquire the invasive phenotype, which enhances the self-renewal and mitochondrial respiration of cancer cells.[41–43] Notably, our data showed that *F. nucleatum*-induced acidification renders a protumorigenic immune microenvironment, which in turn causes cell malignant transformation in the periphery of colonies. This immunomodulatory role of *F. nucleatum* in OSCC invasion is exactly different from the direct protumorigenic effect of other oral bacteria, *P. gingivalis* for example. These data systematically explain why cancer stem cells are predominately located in the periphery,[44] which may be closely associated with microbiota aggregation. Moreover, the lactate-based acidic microenvironment is more beneficial for bacterial reproduction, which forms a

ANOVA *P* = 0.0004; BECLIN1, ANOVA *P* = 0.0016. (F) Glucose consumption (left) and lactate production (right) in CAL27 cells under *F. nucleatum* infection with or without PNA treatment. (one-way-ANOVA), Glucose, ANOVA *P* = 1.9E-07; Lactate, ANOVA *P* = 3.8E-08. (G and H) Confocal images of GLUT1 (green), LAMP1 (red), DIL-labelled cellular membrane (red) and cellular nuclei (blue) in CAL27 cells under *F. nucleatum* infection for 12 h and 24 h pretreated by PNA solution for localization of cellular GLUT1. (I) Western blot analysis of key components in AKT/mTOR pathway in CAL27 cells treated by *F. nucleatum* suspension or PNA solution. (one-way-ANOVA), P-AKT, ANOVA *P* = 2.3E-06; p-mTOR, ANOVA *P* = 0.0003. (J) Western blot analysis of GLUT1, BECLIN1 and ATG5 in CAL27 cells under *F. nucleatum*, SC79 or 3BDO treatment. GAPDH was used as the loading control. GLUT1, (one-way-ANOVA), ANOVA *P* = 0.0002; BECLIN1, ANOVA *P* = 2.0E-09; ATG5, ANOVA *P* = 0.0001.

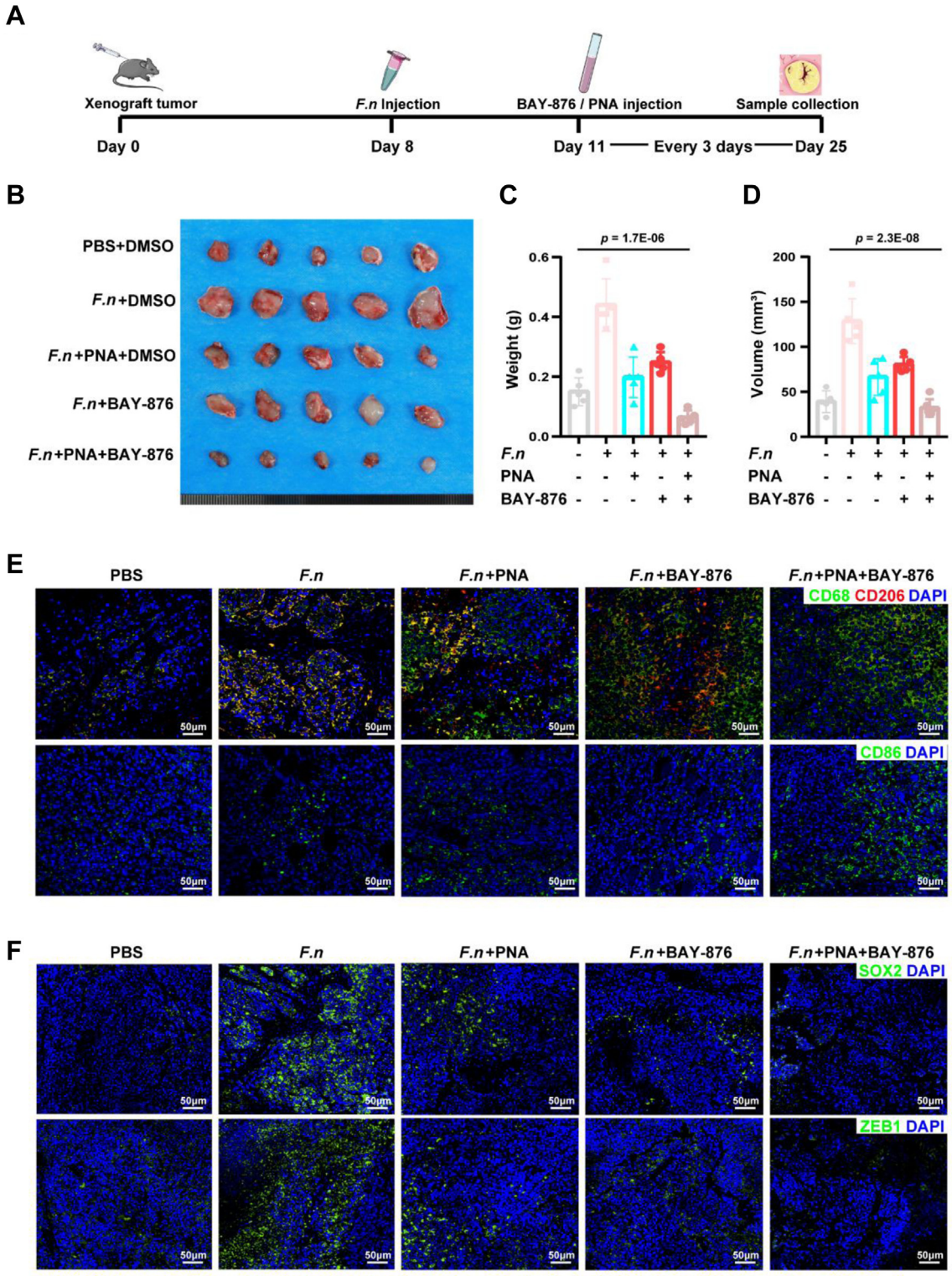

***Fig. 7*: Double targeting at GalNAc and GLUT1 inhibits OSCC progression.** (A) Workflow diagram for translational medical research using BAY-876 and PNA for treatment of OSCC. (B) Representative images of xenograft tumors in C3H mice bearing SCC-7 cells in different groups. Local injection of *F. nucleatum* was used for *in vivo F. nucleatum*-associated tumor model, and injection of PNA, BAY-876 and a combination of them were applied as a different therapeutic strategy. (C and D) Statistical analysis of mouse tumor weights (C) and volumes (D) in different

feedback mechanism for two-way mutual benefit for microbiota colonization and tumor invasion. These data thus provide us new insights into the protumorigenic function of *F. nucleatum*.

The relevant reports highlight that *F. nucleatum* drives cell proliferation and epithelial–mesenchymal transition of colorectal cancer and other tumors mainly by directly regulating cancer cell metabolism, ultimately supporting cell growth.[9,18,19] Besides, the tumor microenvironment has also been identified to play a determinative role in fostering tumor growth and metastasis.[45,46] Here, we confirmed that *F. nucleatum* colonized in OSCC tissues could induce cancer cells to produce much more lactate via the GalNAc-Autophagy-TBC1D5-GLUT1 signaling axis. TBC1D5 degradation leads to GLUT1 localization on the cell surface and glucose uptake, which is metabolized to lactate, subsequently promoting M2-like TAMs formation. Long-term and excessive accumulation of lactate forms a protumorigenic local environment and actively contributes to immune evasion, a cancer hallmark, by directly recruiting and inducing TAMs.[47] The activated TAMs account for more than 70% of the pro-tumor effect caused by *F. nucleatum* in OSCC, which does not precisely overlap with that in colorectal cancer.[17] Due to the "field cancerization" characterization of OSCC, over 600 bacterial species are endemic to the oral cavity.[48,49] OSCC has a complex tumor microenvironment composed of multiple cell types, including cancer-associated fibroblasts, neutrophils, regulatory T cells, macrophages, etc.[50,51] Especially, macrophages make up nearly 50% of the cell population in the tumor stroma, which displays a pro-tumor phenotype to favor OSCC progression.[52–55] Moreover, we noticed that GLUT1 is the key rate-limiting factor of glycolysis in OSCC cells, which differs from some other tumors where rate-limiting enzymes of glycolysis play the leading role.[56,57] Therefore, tissue heterogeneity should be noticed in exploring the functions of tumor-resident microbiota.

The unique roles of *F. nucleatum* provide novel therapeutic targets for advanced OSCC. Some bioengineering strategies have been established for *F. nucleatum*-targeted eradication. Broad-spectrum antibiotic metronidazole was applied earlier for the eradication of *F. nucleatum*.[34,58] Dong X., et al. have constructed a bioinorganic hybrid bacteriophage loaded with Ag nanoparticles for targeted clearance of *F. nucleatum*.[59] In addition, the *F. nucleatum*-specific phage-guided method has also been applied for accurate clearance of *F. nucleatum* to modulate microbiota in colorectal cancer.[60] Nevertheless, *F. nucleatum* is an oral commensal flora, and its eradication is bound to lead to the imbalance of oral microbiota.[61] This study shows that GalNAc and GLUT1 are the two key cytomembrane proteins in *F. nucleatum* promoting tumor invasion, which serve as the ideal biomarkers for immunotherapy for OSCC. Theoretically, single targeting of either GalNAc or GLUT1 can achieve a curative effect in OSCC models. However, since the inhibitors of both GalNAc and GLUT1 are off-target with a certain probability, the strategy of the single-site block is not available for completely inhibiting *F. nucleatum* signaling.[47] Therefore, we propose a dual-targeted therapy, which can achieve a synergistic anticancer effect under the simultaneous intervention of GalNAc and GLUT1 with PNA and BAY-876. By this double-targeted therapy, host macrophages are still attracted to the tumor microenvironment due to ectopic *F. nucleatum*. The loss of the lactate-formed pro-tumor microenvironment hinders macrophages from transforming into M2-like. Most of them even transfer into M1-like anti-tumor macrophages, which remodels an anti-tumor immune microenvironment. This 'convert enemies into friends' strategy can reverse the pro-tumor effect of *F. nucleatum* into a beneficial anti-tumor role, which initiates a persistent anticancer immunity to kill tumor cells. PNA, a natural substance derived from plants, showed its specific anti-tumor function against *F. nucleatum*-associated OSCC. Coincidentally, another type of medicine made from natural components, traditional Chinese medicine (TCM), has nowadays become a novel choice for bacteria-associated tumor treatment. TCM showed superior biocompatibility, less side-effects with lower cost of production, and could mitigate potential drug resistance, advantages of which might suitably be applied in treatment of bacteria-related carcinomas in the future. With the development of TCM extraction and purification, next-generation cancer targeted drugs derived from TCM extracts could exert a much more precise and effective medical intervention.

In conclusion, our research elucidates the landscape of tumor-resident microbiota in tumor progression. *F. nucleatum* is a critical player in regulating the protumorigenic immune microenvironment through GLUT1-driven lactate production, and intervention of *F. nucleatum* provides a novel targeted strategy for patients with advanced OSCC. However, the current perspective for tumor-associated bacteria is limited, as how mutual communications of located cells and colonized bacteria could affect and reshape the tumor microenvironment requires further elucidation. Thus, further exploration for explaining

groups. n = 5/group. (one-way-ANOVA), Weight, ANOVA *P* = 1.7E-06; Volume, ANOVA *P* = 2.3E-08. (E) Representative images of CD68+ CD206+ M2-like TAMs (above) and CD86+ M1-like anti-tumor macrophages (below) in xenograft tumor samples from different groups. (F) Representative images of SOX2 (above) and ZEB1 (below) in xenograft tumor samples from different groups.

interactive communications among stromal cells and bacteria, is necessary for better understanding of microbe-associated tumors and developing novel medical strategies.

Contributors

Study conceptualization: Lili Chen, Qingming Tang, Qian Wan and Jiwei Sun. Data curation: Jiwei Sun, Qingming Tang, Keqi Wo, Haoqi Lei, Junyuan Zhang. Formal analysis: Jiwei Sun, Mengru Xie, Guangjin Chen, Ying Yin, Xiaofei Huang, Keqi Wo, Haoqi Lei, Junyuan Zhang. Funding acquisition: Lili Chen. Supervision: Lili Chen, Qingming Tang. Visualisation: Jiwei Sun, Shaoling Yu, Mengru Xie, Ying Yin, Wenhao Zheng, Guangjin Chen, Xiaofei Huang. Writing – original draft: Jiwei Sun, Qingming Tang, Haoqi Lei. Writing – review & editing: Jiwei Sun, Qingming Tang, Qian Wan, Junyuan Zhang. Lili Chen, Qingming Tang and Jiwei Sun had full access to all the data in the study and take responsibility for the accuracy and integrity of the work. Lili Chen was responsible for the decision to submit the manuscript. All authors read and approved the final version of the manuscript.

Data sharing statement

Data presented as part of this manuscript are available from the corresponding author upon request. Please contact Lili Chen at chenlili1030@hust.edu.cn with requests and inquiries.

Declaration of interests

All authors included in this research declare no competing interests.

Acknowledgments

This project was supported in part by grants from the National Natural Science Foundation of China for Key Program Projects (82030070, to LC) and Distinguished Young Scholars (31725011, to LC), Innovation Team Project of Hubei Province (2020CFA014, to LC).

We thank Dr Hanjiang Wu at the Department of Oral and Maxillofacial Surgery, The Second Xiangya Hospital, Central South University, Changsha for providing clinical OSCC samples and patient information.

Appendix A. Supplementary data

Supplementary data related to this article can be found at https://doi.org/10.1016/j.ebiom.2023.104444.

References

1 Wang W, Adeoye J, Thomson P, Choi SW. Statistical profiling of oral cancer and the prediction of outcome. *J Oral Pathol Med*. 2021;50:39–46.
2 Hanna GJ, O'Neill AJ, Shin KY, et al. Neoadjuvant and adjuvant nivolumab and lirilumab in patients with recurrent, resectable squamous cell carcinoma of the head and neck. *Clin Cancer Res*. 2022;28:468–478.
3 Yang SY, Li SH, Liu JL, et al. Histopathology-based diagnosis of oral squamous cell carcinoma using deep learning. *J Dent Res*. 2022;101:1321, 220345221089858.
4 Tang Q, Cheng B, Xie M, et al. Circadian clock gene Bmal1 inhibits tumorigenesis and increases paclitaxel sensitivity in tongue squamous cell carcinoma. *Cancer Res*. 2017;77:532–544.
5 Chinn SB, Myers JN. Oral cavity carcinoma: current management, controversies, and future directions. *J Clin Oncol*. 2015;33:3269–3276.
6 Banerjee S, Tian T, Wei Z, et al. Distinct microbial signatures associated with different breast cancer types. *Front Microbiol*. 2018;9:951.
7 Buchta Rosean C, Bostic RR, Ferey JCM, et al. Preexisting commensal dysbiosis is a host-intrinsic regulator of tissue inflammation and tumor cell dissemination in hormone receptor-positive breast cancer. *Cancer Res*. 2019;79:3662–3675.
8 Riquelme E, Zhang Y, Zhang L, et al. Tumor microbiome diversity and composition influence pancreatic cancer outcomes. *Cell*. 2019;178:795–806.e712.
9 Yu T, Guo F, Yu Y, et al. Fusobacterium nucleatum promotes chemoresistance to colorectal cancer by modulating autophagy. *Cell*. 2017;170:548–563.e516.
10 Cheung KJ, Padmanaban V, Silvestri V, et al. Polyclonal breast cancer metastases arise from collective dissemination of keratin 14-expressing tumor cell clusters. *Proc Natl Acad Sci U S A*. 2016;113:E854–E863.
11 Yang SF, Lin CW, Chuang CY, et al. Host genetic associations with salivary microbiome in oral cancer. *J Dent Res*. 2022;101:590–598.
12 Vyhnalova T, Danek Z, Gachova D, Linhartova PB. The role of the oral microbiota in the etiopathogenesis of oral squamous cell carcinoma. *Microorganisms*. 2021;9:1549.
13 Healy CM, Moran GP. The microbiome and oral cancer: more questions than answers. *Oral Oncol*. 2019;89:30–33.
14 La Rosa GRM, Gattuso G, Pedullà E, et al. Association of oral dysbiosis with oral cancer development. *Oncol Lett*. 2020;19:3045–3058.
15 McIlvanna E, Linden GJ, Craig SG, Lundy FT, James JA. Fusobacterium nucleatum and oral cancer: a critical review. *BMC Cancer*. 2021;21:1212.
16 Chen S, Zhang L, Li M, et al. Fusobacterium nucleatum reduces METTL3-mediated m(6)A modification and contributes to colorectal cancer metastasis. *Nat Commun*. 2022;13:1248.
17 Abed J, Emgård JE, Zamir G, et al. Fap2 mediates Fusobacterium nucleatum colorectal adenocarcinoma enrichment by binding to tumor-expressed Gal-GalNAc. *Cell Host Microbe*. 2016;20:215–225.
18 Yang Y, Weng W, Peng J, et al. Fusobacterium nucleatum increases proliferation of colorectal cancer cells and tumor development in mice by activating toll-like receptor 4 signaling to nuclear factor-κB, and up-regulating expression of MicroRNA-21. *Gastroenterology*. 2017;152:851–866.e824.
19 Zhang S, Li C, Liu J, et al. Fusobacterium nucleatum promotes epithelial-mesenchymal transiton through regulation of the lncRNA MIR4435-2HG/miR-296-5p/Akt2/SNAI1 signaling pathway. *FEBS J*. 2020;287:4032–4047.
20 Zhou J, Liu L, Wu P, Zhao L, Wu Y. Fusobacterium nucleatum accelerates atherosclerosis via macrophage-driven aberrant proinflammatory response and lipid metabolism. *Front Microbiol*. 2022;13:798685.
21 Pollard JW. Tumour-educated macrophages promote tumour progression and metastasis. *Nat Rev Cancer*. 2004;4:71–78.
22 Huang Y, Motta E, Nanvuma C, et al. Microglia/macrophage-derived human CCL18 promotes glioma progression via CCR8-ACP5 axis analyzed in humanized slice model. *Cell Rep*. 2022;39:110670.
23 Tang Q, Xie M, Yu S, et al. Periodic oxaliplatin administration in synergy with PER2-mediated PCNA transcription repression promotes chronochemotherapeutic efficacy of OSCC. *Adv Sci*. 2019;6:1900667.
24 Newcombe RG. Two-sided confidence intervals for the single proportion: comparison of seven methods. *Stat Med*. 1998;17:857–872.
25 Rodríguez Del Águila M, González-Ramírez A. Sample size calculation. *Allergol Immunopathol*. 2014;42:485–492.
26 Perera M, Al-Hebshi NN, Perera I, et al. Inflammatory bacteriome and oral squamous cell carcinoma. *J Dent Res*. 2018;97:725–732.
27 Zhao H, Chu M, Huang Z, et al. Variations in oral microbiota associated with oral cancer. *Sci Rep*. 2017;7:11773.
28 Wang XM, Zhang Z, Pan LH, Cao XC, Xiao C. KRT19 and CEACAM5 mRNA-marked circulated tumor cells indicate unfavorable prognosis of breast cancer patients. *Breast Cancer Res Treat*. 2019;174:375–385.
29 Roy S, Leidal AM, Ye J, Ronen SM, Debnath J. Autophagy-dependent shuttling of TBC1D5 controls plasma membrane translocation of GLUT1 and glucose uptake. *Mol Cell*. 2017;67:84–95.e85.
30 Rubinstein MR, Wang X, Liu W, et al. Fusobacterium nucleatum promotes colorectal carcinogenesis by modulating E-cadherin/β-catenin signaling via its FadA adhesin. *Cell Host Microbe*. 2013;14:195–206.
31 Hofmann BT, Picksak AS, Kwiatkowski M, et al. Truncated O-GalNAc glycans impact on fundamental signaling pathways in pancreatic cancer. *Glycobiology*. 2021:cwab088.
32 Fu A, Yao B, Dong T, et al. Tumor-resident intracellular microbiota promotes metastatic colonization in breast cancer. *Cell*. 2022;185:1356–1372.e1326.
33 Meyerson M. Bacterial invaders drive CRC progression. *Sci Signal*. 2020;13:eabc4218.

34 Parhi L, Alon-Maimon T, Sol A, et al. Breast cancer colonization by Fusobacterium nucleatum accelerates tumor growth and metastatic progression. *Nat Commun*. 2020;11:3259.
35 Thomas AM, Manghi P, Asnicar F, et al. Metagenomic analysis of colorectal cancer datasets identifies cross-cohort microbial diagnostic signatures and a link with choline degradation. *Nat Med*. 2019;25:667–678.
36 Kawasaki M, keda Y, Ikeda E, et al. Oral infectious bacteria in dental plaque and saliva as risk factors in patients with esophageal cancer. *Cancer*. 2021;127:512–519.
37 Alon-Maimon T, Mandelboim O, Bachrach G. Fusobacterium nucleatum and cancer. *Periodontol 2000*. 2022;89:166–180.
38 Datorre JG, de Carvalho AC, Guimarães DP, Reis RM. The role of Fusobacterium nucleatum in colorectal carcinogenesis. *Pathobiology*. 2021;88:127–140.
39 Mima K, Nishihara R, Qian ZR, et al. Fusobacterium nucleatum in colorectal carcinoma tissue and patient prognosis. *Gut*. 2016;65:1973–1980.
40 Hsieh YY, Tung SY, Pan HY, et al. Fusobacterium nucleatum colonization is associated with decreased survival of helicobacter pylori-positive gastric cancer patients. *World J Gastroenterol*. 2021;27:7311–7323.
41 Jin Z, Yue Q, Duan W, et al. Intelligent SERS navigation system guiding brain tumor surgery by intraoperatively delineating the metabolic acidosis. *Adv Sci*. 2022;9:e2104935.
42 Hu P, Li S, Tian N, et al. Acidosis enhances the self-renewal and mitochondrial respiration of stem cell-like glioma cells through CYP24A1-mediated reduction of vitamin D. *Cell Death Dis*. 2019;10:25.
43 Bohn T, Rapp S, Luther N, et al. Tumor immunoevasion via acidosis-dependent induction of regulatory tumor-associated macrophages. *Nat Immunol*. 2018;19:1319–1329.
44 Biddle A, Liang X, Gammon L, et al. Cancer stem cells in squamous cell carcinoma switch between two distinct phenotypes that are preferentially migratory or proliferative. *Cancer Res*. 2011;71:5317–5326.
45 Hinshaw DC, Shevde LA. The tumor microenvironment innately modulates cancer progression. *Cancer Res*. 2019;79:4557–4566.
46 Ning WR, Jiang D, Liu XC, et al. Carbonic anhydrase XII mediates the survival and prometastatic functions of macrophages in human hepatocellular carcinoma. *J Clin Invest*. 2022;132:e153110.
47 Hayes C, Donohoe CL, Davern M, Donlon NE. The oncogenic and clinical implications of lactate induced immunosuppression in the tumour microenvironment. *Cancer Lett*. 2021;500:75–86.
48 Karpiński TM. Role of oral microbiota in cancer development. *Microorganisms*. 2019;7:20.
49 Hashim D, Genden E, Posner M, Hashibe M, Boffetta P. Head and neck cancer prevention: from primary prevention to impact of clinicians on reducing burden. *Ann Oncol*. 2019;30:744–756.
50 Peltanova B, Raudenska M, Masarik M. Effect of tumor microenvironment on pathogenesis of the head and neck squamous cell carcinoma: a systematic review. *Mol Cancer*. 2019;18:63.
51 Niklander SE. Inflammatory mediators in oral cancer: pathogenic mechanisms and diagnostic potential. *Front Oral Health*. 2021;2:642238.
52 Chiu KC, Lee CH, Liu SY, et al. Polarization of tumor-associated macrophages and Gas6/Axl signaling in oral squamous cell carcinoma. *Oral Oncol*. 2015;51:683–689.
53 Wehrhan F, Büttner-Herold M, Hyckel P, et al. Increased malignancy of oral squamous cell carcinomas (oscc) is associated with macrophage polarization in regional lymph nodes–an immunohistochemical study. *BMC Cancer*. 2014;14:522.
54 Vitale I, Manic G, Coussens LM, Kroemer G, Galluzzi L. Macrophages and metabolism in the tumor microenvironment. *Cell Metab*. 2019;30:36–50.
55 Petruzzi MN, Cherubini K, Salum FG, de Figueiredo MA. Role of tumour-associated macrophages in oral squamous cells carcinoma progression: an update on current knowledge. *Diagn Pathol*. 2017;12:32.
56 Sun X, Peng Y, Zhao J, et al. Discovery and development of tumor glycolysis rate-limiting enzyme inhibitors. *Bioorg Chem*. 2021;112:104891.
57 Zhu S, Guo Y, Zhang X, et al. Pyruvate kinase M2 (PKM2) in cancer and cancer therapeutics. *Cancer Lett*. 2021;503:240–248.
58 Bullman S, Pedamallu CS, Sicinska E, et al. Analysis of Fusobacterium persistence and antibiotic response in colorectal cancer. *Science (New York, NY)*. 2017;358:1443–1448.
59 Dong X, Pan P, Zheng DW, et al. Bioinorganic hybrid bacteriophage for modulation of intestinal microbiota to remodel tumor-immune microenvironment against colorectal cancer. *Sci Adv*. 2020;6:eaba1590.
60 Zheng DW, Dong X, Pan P, et al. Phage-guided modulation of the gut microbiota of mouse models of colorectal cancer augments their responses to chemotherapy. *Nat Biomed Eng*. 2019;3:717–728.
61 Stokowa-Sołtys K, Wojtkowiak K, Jagiełło K. Fusobacterium nucleatum–friend or foe? *J Inorg Biochem*. 2021;224:111586.